Astronomy & Astrophysics manuscript no. output
July 15, 2026

Extreme color–magnitude variability: Connection to changing-look active galactic nuclei

Litao Zhu[1], Zhongxiang Wang[1], Alok C. Gupta[2], P. U. Devanand[2], Ruoheng Yang[1], Qiangmeng Huang[1], Man Lang[1], and Jiawen Li[1]

[1] Department of Astronomy, School of Physics and Astronomy, Key Laboratory of Astroparticle Physics of Yunnan Province, Yunnan University, Kunming 650091, China
e-mail: zhulitao@mail.ynu.edu.cn, wangzx20@ynu.edu.cn
[2] Aryabhatta Research Institute of Observational Sciences (ARIES), Manora Peak, Nainital - 263 001, India

ABSTRACT

Context. Changing-look active galactic nuclei (CL-AGNs) challenge the unified model of AGNs and offer key insights into the physics of the accretion processes of super-massive black holes. While systematic spectroscopic comparisons have successfully identified large samples of CL-AGNs, photometric selection based on variability features provides an efficient alternative.
Aims. We used the color–magnitude (CM) variability pattern method to continue our identification of the CL transition in AGNs. The resulting CL-AGN sample can help improve understanding of this phenomenon.
Methods. The CM variability pattern method utilizes the slope (k) of the CM variations to identify strong "bluer-when-brighter" behavior, while the variation amplitudes in optical and mid-infrared (MIR) bands are also considered. The candidates selected from the Type-2 AGNs given in the Sloan Digital Sky Survey catalog were spectroscopically observed by us using the 3.6-m Devasthal Optical Telescope and the 2-m Himalayan Chandra Telescope.
Results. We successfully confirm seven turn-on CL-AGNs among 12 candidates in this work. Compared with both the general AGN populations and the spectroscopically identified CL-AGN sample, these CL-AGNs show larger optical and MIR variations and k values. The extreme CM variabilities of these sources (with optical magnitude changes > 0.9) occurred recently. For four sources, flare-like brightening episodes were temporally associated with turn-on transitions within 3–7 years, suggesting that these flares may trace short-timescale accretion enhancement, central brightening, and broad-line region re-illumination. In addition, the estimated Eddington ratios for the confirmed CL-AGNs appear to cluster around a critical value of $\lambda_{\rm Edd} \sim 0.01$.
Conclusions. The extreme CM variability serves as a highly efficient criterion for finding CL-AGNs. The properties of the CL-AGNs thus found suggest that they may represent AGNs at a pivotal state, which likely occurs in CL transitions due to enhanced accretion activity, while the cause of the accretion activity, which was determined to have a timescale of several years in this work, remains to be investigated further.

Key words. galaxies: active – quasars: emission lines – Active galactic nuclei – Optical flares

1. Introduction

Active galactic nuclei (AGNs) are classified into two major categories based on their ultraviolet and optical spectral features: Type 1 AGNs, which exhibit both broad emission lines (BELs) and narrow emission lines, and Type 2 AGNs, which show only narrow emission lines. Under the standard unification scheme, this dichotomy is governed primarily by an observer's viewing angle relative to an optically thick, dusty torus that surrounds the central supermassive black hole (SMBH). In Type 2 AGNs, their broad-line regions (BLRs) are obscured, while in Type 1s, their BLRs are visible (e.g., Lawrence 1987; Antonucci 1993; Urry & Padovani 1995; Tadhunter 2008). However, this static orientation-based paradigm has been challenged by the discovery of the changing-look (CL) phenomenon, which describes how AGNs can undergo drastic spectral transitions between the two main types. Such transitions are marked by the appearance or disappearance of BELs and sometimes also involve intermediate subtypes such as Types 1.2, 1.5, 1.8, and 1.9 (defined by the flux ratios of Hβ and Hα relative to [O III]; Osterbrock 1981; Winkler 1992). The initial instances of the CL transitions were reported decades ago in individual sources (e.g., Tohline & Osterbrock 1976; Cohen et al. 1986; Storchi-Bergmann et al. 1993; Aretxaga et al. 1999; Eracleous & Halpern 2001; Denney et al. 2014; Shappee et al. 2014; LaMassa et al. 2015). However, the advent of large-area time-domain photometric and spectroscopic surveys in recent years has enabled the discovery of a growing population of these transition events, transforming the studies from accidental discoveries to systematic analyses (e.g., Ruan et al. 2016; Runnoe et al. 2016; Gezari et al. 2017; Yang et al. 2018; Ross et al. 2020; Zhu et al. 2024; Guo et al. 2024, 2025).

Changing-look transitions often occur on timescales of a few years, and their physical driver is a subject of intense debate. The standard α-disk model predicts that global changes in the accretion flow should occur on the viscous timescale, which is typically on the order of 10^4–10^5 years for those of SMBHs (e.g., Lawrence 2018). While variable obscuration by moving dusty clouds offers a possible solution (e.g., Elitzur 2012), mounting evidence from mid-infrared (MIR) dust echoes and continuum reverberation mapping favors the causes due to intrinsic variations in the accretion rate or state transitions analogous to those in X-ray binaries (e.g., Noda & Done 2018; Ruan et al. 2019; liu et al. 2019; Ai et al. 2020; Gilbert et al. 2025). Con-

Article published by EDP Sciences, to be cited as https://doi.org/10.1051/0004-6361/202661111

sequently, CL-AGNs provide a unique, real-time laboratory to probe the physics of accretion instabilities, the activity cycles of active nuclei, and the dynamical connection between the central accretion-powered engine and the BLR.

Systematic searches for CL-AGNs have primarily followed two distinct pathways. The first relies on direct comparison of multi-epoch spectra from either cross-matching data of different surveys (e.g., Yang et al. 2018; Guo et al. 2024; Dong et al. 2025; Guo et al. 2025; Liu et al. 2026) or analyzing repeated observations within a single survey (e.g., Green et al. 2022; Zeltyn et al. 2024; Chen et al. 2025). While definitive, this approach is limited by the scarcity of spectroscopic epochs. The second involves preselections of candidates based on photometric variability characteristics. The process screens for high-amplitude variations in optical (e.g., MacLeod et al. 2016; Frederick et al. 2019; Graham et al. 2020; Wang et al. 2024; Yang et al. 2025; Verrico et al. 2026) or MIR bands (e.g., Sheng et al. 2020; Wang et al. 2023) and follows this with spectroscopic observations for confirmation. Such efforts have also recently expanded to incorporate applications of machine learning algorithms (e.g., López-Navas et al. 2022, 2023).

Among the preselection methods, we have developed a color–magnitude (CM) pattern method that combines variability amplitude with the CM slope (parameterized as k).[1] By explicitly targeting sources that follow a steep bluer-when-brighter (BWB) trend in the optical CM space, this method can effectively identify high-probability candidates of turn-on CL-AGNs (Zhu et al. 2025). The photometric data used to construct the CM diagrams for candidate selections were mainly from the Zwicky Transient Facility (ZTF; Bellm et al. 2019), which started its survey from approximately 2018. Thus, we were essentially monitoring a large number of AGNs with the ZTF light curve data to select those AGNs showing significant variations (optical changes >0.9 mag) and strong BWB trends ($k \geq 0.1$; Zhu et al. 2025). The CL transitions we have identified as a result likely occurred after 2018, i.e., in less than 8 years.

Here, we continue our CL-AGN identification work applying the CM variability pattern method. In particular, we conducted spectroscopic observations in 2024–2025 and compared the obtained spectra with those from the Sloan Digital Sky Survey (SDSS; Abazajian et al. 2009). Seven CL-AGNs were identified from 12 selected candidates. Among those identified, two (J115953+051330 and J134330+510204) were reported by Guo et al. (2025) as CL-AGNs, but we were not aware of this fact at the time of our observations. Furthermore, by adding spectra for comparison from the Large Sky Area Multi-Object Fiber Spectroscopic Telescope (LAMOST; Cui et al. 2012) and the Dark Energy Spectroscopic Instrument (DESI; DESI Collaboration et al. 2016), we were able to determine the occurrence times for four cases of the CL transitions to within 3–7 years, during which flaring activity with extreme CM variability was seen. The identification study we conducted thus provides a potential clue for the connection between the extreme variability and the CL transition.

This paper is organized as follows: In Sec. 2 we describe the candidate CL-AGN sample and the data reduction. Sec. 3 presents the spectroscopic confirmation results and the related property-analysis results. In Sec. 4 we discuss the details in this identification work and possible physical interpretations of the results. Throughout this paper, we adopted cosmological parameters from the Planck mission (Planck Collaboration et al. 2020): $H_0 = 67.4\,\mathrm{km\,s^{-1}\,Mpc^{-1}}$ and $\Omega_m = 0.315$.

[1] The CM slope is defined as $zg - zr = k\,zr + c$, where zg and zr are magnitudes in two bands, obtained nearly simultaneously, and c is the intercept.

2. Selection of candidate CL-AGNs and observations

2.1. Candidate CL-AGN selection

We adopted the CM variability pattern method proposed in (Zhu et al. 2025) to select CL-AGN candidates. This method relies on the CM slope parameter, k, derived from the linear fit of $zg - zr$ versus zr, where zg and zr are the g- and r-band magnitudes of a source from the ZTF survey and $zg-zr$ is calculated from the two magnitudes obtained within one day. Linear regression was performed as a weighted least-squares fit with the Python package `iminuit`. The uncertainty of each color value, estimated from the ZTF photometric errors, was used as the fit weight, and the quoted uncertainty of k is the corresponding 1σ fit error. A large k value indicates an AGN exhibiting strong BWB variability, a feature characteristic of Type 1 AGNs.

The parent sample was constructed based on the spectral classifications of AGNs from Data Release 16 (DR16; Ahumada et al. 2020) of SDSS. In addition to the CM diagrams constructed from ZTF photometric data, MIR light curves from Near-Earth Object WISE (NEOWISE; Mainzer et al. 2011; WISE Team 2020) data from the Wide-field Infrared Survey Explorer (WISE; Wright et al. 2010) were also constructed. Specifically the MIR light curves are at WISE $W1$ (3.4 μm) and $W2$ (4.6 μm) bands, which presumably trace the dust echo responses to the optical variability of AGNs.

Focusing on the spectroscopically identified Type 2 sources in the sample (for details see Zhu et al. 2025), we selected sources with more significant variability as the candidates, as they have likely undergone CL transitions. As we learned from previous work in Zhu et al. (2025), the requirements are a magnitude change in the zg band of $\Delta zg > 0.9$ mag and in the W2 band of $\Delta W2 > 0.4$ mag. The selection resulted in 12 candidates for our spectroscopic confirmation observations. In the selection, we did not consider K-corrections. The redshifts of the sources are generally not high, and the selection results are not changed by whether or not we add the K-corrections. The variability properties of these selected sources are summarized in Table 1. The last two columns of the table provide the Spearman's rank correlation coefficient (ρ_S) and the corresponding two-sided p_S value for each CM relation. The positive ρ_S values and small p_S values served as a check for supporting the reliability of the fit CM slopes (k) that were used in our selection.

2.2. Spectroscopic observations and spectral analysis

2.2.1. Observations and data reduction

Spectroscopic observations of the 12 targets were conducted using two telescopes: the 3.6-m Devasthal Optical Telescope (DOT; Omar et al. 2019) and the 2-m Himalayan Chandra Telescope (HCT; Cowsik et al. 2002). The information for the observations is given in Table A.1.

For the observations with DOT, we utilized the ARIES-Devasthal Faint Object Spectrograph and Camera (ADFOSC). The instrument is equipped with a 4096 × 4096 pixel CCD detector. We employed the 132R-600gr/mm grism, which provides a spectral dispersion of $\sim$ 0.10 nm pixel^{-1} and covers a wavelength range of 350–700 nm. A long slit with a width of 2.0″

Table 1: Variability metrics for all observed sources.

Name	Δzg	Δzr	$\Delta W1$	$\Delta W2$	k	ρ_S	p_S
Confirmed CL AGN							
J014638+131109	1.249 ± 0.062	0.864 ± 0.035	0.359 ± 0.022	0.480 ± 0.045	0.46 ± 0.02	0.324	4.6×10^{-10}
J115953+051330	0.963 ± 0.022	0.714 ± 0.018	0.697 ± 0.011	0.927 ± 0.017	0.27 ± 0.02	0.428	5.0×10^{-7}
J121228+501412	1.151 ± 0.082	0.785 ± 0.042	0.667 ± 0.016	0.930 ± 0.031	0.20 ± 0.03	0.152	6.0×10^{-4}
J131101+000310	1.042 ± 0.032	0.769 ± 0.022	0.629 ± 0.014	0.849 ± 0.025	0.55 ± 0.02	0.388	2.9×10^{-8}
J134330+510204	1.094 ± 0.044	0.694 ± 0.026	0.647 ± 0.011	0.784 ± 0.019	0.46 ± 0.01	0.140	1.1×10^{-4}
J152502+110744	1.723 ± 0.063	1.075 ± 0.042	0.755 ± 0.015	0.643 ± 0.021	0.641 ± 0.007	0.861	1.6×10^{-10}
J160626+044802	1.297 ± 0.060	0.971 ± 0.029	0.467 ± 0.015	0.677 ± 0.035	0.45 ± 0.02	0.338	3.6×10^{-10}
Other candidate							
J075846+270515	1.042 ± 0.025	0.804 ± 0.018	0.616 ± 0.013	0.993 ± 0.054	0.250 ± 0.007	0.537	3.9×10^{-10}
J105344+492955	0.945 ± 0.023	0.648 ± 0.018	0.201 ± 0.011	0.618 ± 0.060	0.22 ± 0.01	0.284	9.6×10^{-10}
J111137+140118	1.219 ± 0.053	0.747 ± 0.041	0.610 ± 0.020	0.644 ± 0.034	0.48 ± 0.02	0.603	1.7×10^{-10}
J111614+061736	1.029 ± 0.034	0.819 ± 0.022	0.761 ± 0.015	1.099 ± 0.037	0.37 ± 0.02	0.572	5.0×10^{-10}
J132558+411500	2.656 ± 0.062	1.982 ± 0.038	1.824 ± 0.017	1.885 ± 0.025	0.185 ± 0.003	0.785	1.9×10^{-10}

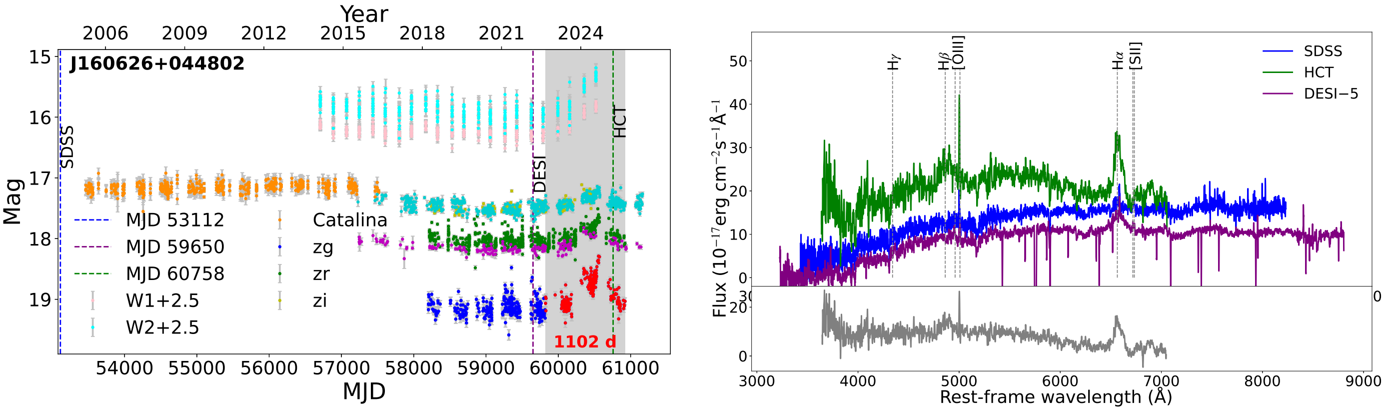

Fig. 1: Light curves and spectra for J160626+044802. The left panel displays the optical and MIR light curves, where a flare determined from the zg-band data is marked in red and its time duration is marked by the gray region. The top-right panel shows the spectra obtained from SDSS, DESI, and HCT (whose epochs are marked by the vertical dashed lines in the left panel), and the bottom-right panel shows the difference spectrum (ours minus the SDSS spectrum; the latter has been convolved with the spectral resolution of ours).

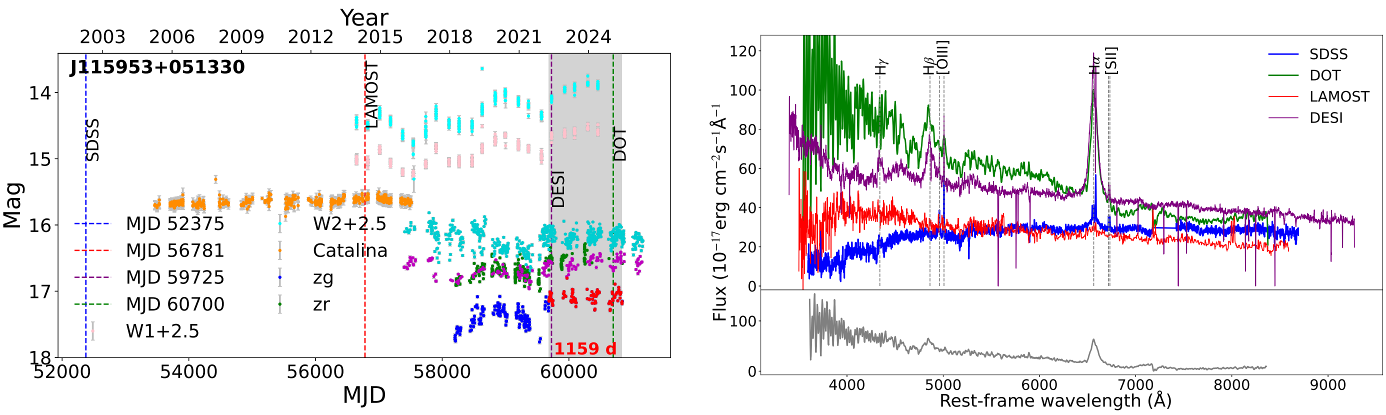

Fig. 2: Same as Fig. 1 but for J115953+051330, except that the bright spectrum was from the DOT observation and an additional LAMOST spectrum was found.

was used. Wavelength calibration was performed using spectra of an iron-neon-argon lamp.

The observations with HCT were carried out using the Hanle Faint Object Spectrograph and Camera. To ensure the coverage of key BELs, such as Hα and Hβ, we set up the instrument based on the specific requirements for obtaining a full spectrum for each target (given its redshift z). We employed Grism 7 (covering ∼3800–6840 Å) paired with a slit of width 0.″77, Grism 8 (covering ∼5800–8350 Å) paired with a slit of width 1.″15, or a combination of both settings when necessary. Similar to the

DOT observations, the wavelength calibration for the HCT spectra was achieved using the spectra of an iron-neon-argon lamp.

The raw spectroscopic data were reduced following the standard procedures by using the IRAF software package. The reduction steps included bias subtraction, flat-fielding, spectral extraction, wavelength calibration, and flux calibration. The standard stars observed and used for flux calibration are listed in Table A.1.

2.2.2. Spectrum data and analysis

We downloaded the SDSS spectra, which were mostly taken more than ten years ago. In addition, we searched the LAMOST and DESI data for our candidates and found a few spectra that were taken more recently. The obtained spectra for two confirmed CL-AGNs are shown in Fig. 1 & 2 as the examples.

To accurately measure the spectral properties of all the spectra, we performed spectral fitting using the Python-based package `QSOFITMORE` (Fu 2021). This package, which extends the `PyQSOFit` framework (Guo et al. 2018), was employed to model the continuum and decompose the emission lines. We obtained precise measurements of the fluxes and the full width at half maximum (FWHM) for key BELs, specifically Hα and Hβ. An example of the spectral fitting is presented in Fig. 3.

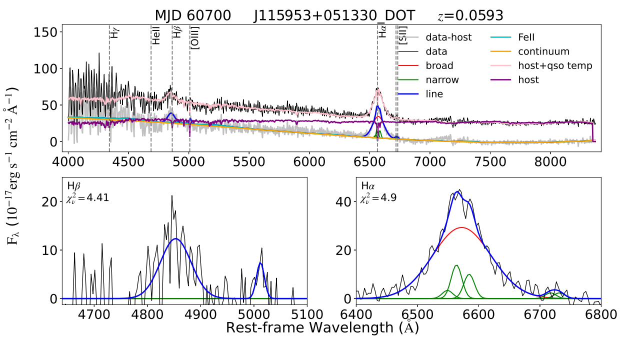

Fig. 3: Example of spectral fitting using `QSOFITMORE` for the DOT spectrum of J115953+051330. The spectrum was corrected for redshift and Galactic extinction, and the host galaxy contribution was subtracted to model the pure quasar emission components and to derive the corresponding parameters. The parameters M_{BH} and λ_{Edd} for this AGN calculated from the fitting parameters are given in Table 2.

For the sources exhibiting a detectable broad Hβ component, we estimated the single-epoch virial black hole (BH) mass ($M_{\rm BH}$) using the empirical scaling relation provided by Vestergaard & Peterson (2006). The estimation follows the formula

$$\log\left(\frac{M_{\rm BH}}{M_\odot}\right) = \log\left[\left(\frac{\rm FWHM(H\beta)}{\rm km\,s^{-1}}\right)^2\left(\frac{L_{5100}}{10^{44}\,\rm erg\,s^{-1}}\right)^{0.5}\right] + 0.91, \quad (1)$$

where L_{5100} represents the monochromatic luminosity at 5100 Å, and FWHM(Hβ) is the line width of the broad Hβ component. Subsequently, we derived the Eddington ratio, defined as $\lambda_{\rm Edd} = L_{\rm bol}/L_{\rm Edd}$, where the Eddington luminosity is $L_{\rm Edd} = 1.3 \times 10^{38}(M_{\rm BH}/M_\odot)\,\rm erg\,s^{-1}$. The bolometric luminosity was estimated as $L_{\rm bol} = 9.26 \times L_{5100}$ by adopting the scaling from (Richards et al. 2006) for quasars with $z < 0.8$.

2.3. Variability analysis

Our selection was primarily based on variability features. To display the long-term variability behavior (e.g., Fig. 1 & Fig. 2), we included archival photometric data from two additional surveys: the V-band data from the Catalina Real-time Transient Survey (CRTS; Drake et al. 2009) and the cyan (ac; 420–650 nm) and orange (ao; 560–820 nm) band data from the Asteroid Terrestrial-impact Last Alert System (ATLAS; Tonry et al. 2018). The constructed light curves of the five confirmed CL-AGNs and five other candidates are provided in the Appendix (Fig. B.1–B.5 and Fig. C.1–C.5, respectively).

The long-term light curves show that the CL-AGNs have undergone significant flux variations in both optical and MIR bands. To quantify these variations, we calculated the maximum amplitude changes: Δzg, Δzr, $\Delta W1$, and $\Delta W2$, which are summarized in Table 1. For the MIR data, the magnitude changes were derived using binned WISE light curves, where data points from one epoch were averaged into one bin. As shown in the table, the CL-AGNs consistently exhibited substantial amplitudes in the Δzg, Δzr, and MIR bands. The basic properties and variability metrics are summarized in Table 1.

By carefully examining the light curves of the candidates, we approximately identified three types of variations: a major flare, as in the light curves of J115953+051330 (Fig. 2), J152502+110744 (Fig. B.5), and J160626+044802 (Fig. 1); one or two intermediate flares, as in those of J132558+411500 (Fig. C.5) and J134330+510204 (Fig. B.4); and flickers, as in those of J014638+131109 (Fig. B.1) and J121228+501412 (Fig. B.2). To understand the role of these variations (in particular the flares) in forming the CM patterns, we applied the Bayesian blocks (BB) algorithm (Scargle et al. 2013), implemented through the Python package Astropy,[2] to zg-band light curves. The median magnitude of an entire light curve was defined as the quiescent baseline. A continuous sequence of blocks significantly brighter than this baseline determined the time interval of a flare. From this analysis we obtained the time interval of a flare for each candidate. The determination relied on the baseline level and the most deviating data point above the baseline, which could result in extreme cases such as a short 169 d flare at the end of the light curve of J121228+501412 (Fig. B.2). In any case, since we were interested in checking how flares or flickers contribute to the CM patterns, we did not adjust the determination for possibly more reasonable results.

To construct CM diagrams, we binned the ZTF zg- and zr-band data points over a 3-day interval, which sometimes helped avoid one data point of a band versus multiple data points of another band. The flares determined above from the BB algorithm were marked in the CM diagrams (Fig D.1 & D.2).

3. Results

Our spectroscopic observations of 12 targets resulted in the successful identification of seven turn-on CL-AGNs. Representative examples of the identified CL-AGNs are presented in Fig. 1 (observed with HCT) and Fig. 2 (observed with DOT). Brief descriptions of the individual CL-AGN sources are presented in the following subsections.

J014638+131109: The early CRTS data for this source were relatively stable. A rising trend appeared in the MIR data starting from 2016. There was a flux-variation dip appearing clearly in zg band after 2021, which was followed by a recovering upward trend. A time period of ~680 d in the first part of the zg

[2] https://docs.astropy.org/en/stable/api/astropy.stats.bayesian_blocks.html

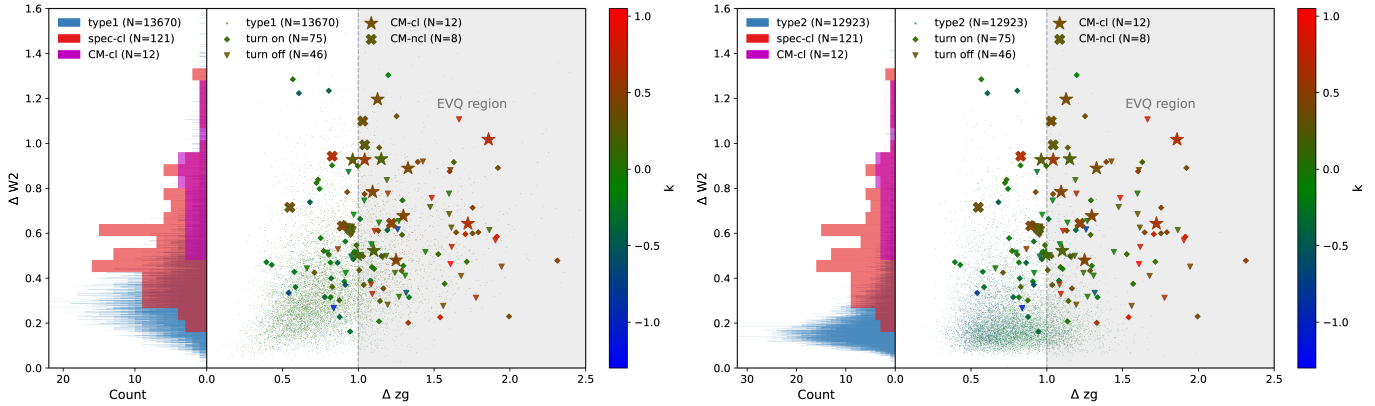

Fig. 4: Distributions of variability amplitudes ($\Delta W2$ versus Δzg) and the color–magnitude slope (k). The upper and lower panels display the general SDSS Type 1 and Type 2 AGN populations as the background, respectively. The color bar on the right of each panel represents the k value. The histograms on the left side of each panel illustrate the distributions of $\Delta W2$. In the plots, "CM-cl" and "CM-ncl" denote the 12 confirmed CL-AGNs and the eight non-confirmed CL candidates, respectively, selected via the CM variability pattern method (including Zhu et al. 2025 and this work). The samples labeled "spec-cl," "turn on," and "turn off" were derived from the currently largest spectroscopically selected CL-AGN catalog from Guo et al. (2025).

Table 2: Properties of the seven CL sources.

Source	z	$\mathrm{Log}(M_{BH}/M_\odot)$	$\mathrm{Log}(\lambda_{Edd})$	Transition
J014638+131109	0.1601	8.17 ± 0.11	-1.80 ± 0.13	Hβ on
J115953+051330	0.0593	7.78 ± 0.17	-1.86 ± 0.19	Hβ on
J121228+501412	0.1700	8.07 ± 0.17	-1.89 ± 0.19	Hβ on
J131101+000310	0.0962	8.24 ± 0.19	-1.72 ± 0.23	Hα, Hβ on
J134330+510204	0.1316	-	-	Hα on
J152502+110744	0.3326	8.42 ± 0.13	-1.54 ± 0.15	Hβ on
J160626+044802	0.1158	8.29 ± 0.25	-1.68 ± 0.29	Hα, Hβ on

light curve was determined to be a flare. Our HCT spectrum was obtained during a relatively bright phase. Compared to the extremely weak broad Hα observed in the earlier SDSS epoch, the HCT spectrum revealed prominent, broad Hα and Hβ lines (Fig B.1).

J115953+051330: The CRTS data for this source did not show significant variability. The more recent ATLAS and ZTF data indicated fluctuations, but the zg-band data suggested a long flare before ~2022 and a stable brightening state after; the latter was identified as a flare with the BB algorithm. The MIR response was aligned with the z_g-band variations, likely as the addition to an overall brightening trend. The LAMOST spectrum taken before 2015 indicates a Type-2 AGN, and the DESI (as already reported in Guo et al. 2025) and our DOT spectra, both obtained during the identified flare, revealed significantly enhanced broad Hα, a fully emerged broad Hβ, and a clear continuum component (Fig 2).

J121228+501412: The MIR light curves of this source showed a continuous dimming trend during ~2015–2017. Starting from ~2019, there was a slow brightening trend particularly visible in zg band. Before the brightening, the LAMOST spectrum revealed a clear absence of broad Hβ and Hγ components, which emerged in our HCT spectrum obtained during the identified short flare (Fig B.2). In addition, comparing the HCT spectrum with the much early SDSS spectrum, the Hα emission appeared to be significantly strengthened. The time duration between the LAMOST and HCT observations is ~6.5 years.

J131101+000310: The variability of this source was mild in the early years until ~2020, when the light curves, particularly at zg band, showed sharp intermediate flares, accompanied with MIR flux increases. The LAMOST spectrum taken at ~2018 and our DOT spectrum taken after the identified optical flares established a CL transition between the epochs of the two spectra (having a time duration of ~7.0 years); the latter displayed a significantly enhanced broad Hα and an emerged broad Hβ (Fig B.3). The transition was likely in association with the flaring activity between the epochs of the two spectra.

J134330+510204: Similar to J131101+000310, this source was relatively quiet in early years, but a noticeable flare occurred in ~2023. The DESI spectrum (already reported in Guo et al. 2025) taken right before the identified flare showed that broad Hα emission had emerged, and the DOT spectrum taken after the flare indicated a stronger broad Hα component (Fig B.4).

J152502+110744: The variability of this source was not intense in the early years. However in late 2020, the optical flux increased significantly, appearing as a major flare and with the zg magnitude up by ~ -1.8 mag. The MIR light curves followed the optical ones. Our HCT spectrum, taken during the brightening stage, exhibited a significantly enhanced continuum and broad Hα component as well as a potentially very broad Hβ component (Fig B.5). The DESI spectrum taken at the onset of the flare, which did not show these features, limited the CL transition to within ~4.0 years.

J160626+044802: This source remained relatively stable in both optical and MIR bands until the appearance of a major flare from ~2022. The early SDSS spectrum was dominated by the galaxy component without obvious BELs, and the DESI spectrum taken right before the flare was similar but showed the appearance of a broad Hα component. In our HCT spectrum taken after the peak of the flare, distinct broad Hα and Hβ emission lines appeared, accompanied by an enhanced continuum component (Fig 1). Similar to J152502+110744, the transition should have been associated with the flare occurring within the ~3.0 years between the DESI and HCT observations.

To place our results in a broader context, we combined the seven CL-AGNs identified in this work with the five CL-AGNs identified previously using the same method (Zhu et al. 2025) and plotted their Δzg and $\Delta W2$ (in Fig. 4); their k values (derived from the CM variations) are also indicated. For comparison, we also plotted the distribution of Type 1 AGNs (left panel of Fig. 4) and Type 2 AGNs (right panel of Fig. 4) from the SDSS DR16 catalog. Furthermore, we included a sample of 121 CL-AGNs from Guo et al. (2025) that have available ZTF and WISE light curve data. As illustrated in Fig. 4, the Type 1 and Type 2 AGNs are clustered in the region characterized by relatively small values of Δzg, $\Delta W2$, and k. The majority of Type 2 AGNs exhibit k values less than zero, whereas Type 1 AGNs are distributed around $k \approx 0$ (see also Zhu et al. 2025). For Type 2 AGNs, we point out that some of their apparent negative k values do not necessarily imply a physical "redder-when-brighter" behavior; rather, they primarily result from unreliable linear fitting caused by the lack of significant intrinsic variability in these objects. The CL-AGNs identified through spectrum comparisons, i.e., the sample in Guo et al. 2025, occupy a region with larger variability amplitudes than those of Type 1/2 AGNs, but notably they are not as large as those of the CL-AGNs found from our CM variability method.

The estimated black hole masses ($M_{\rm BH}$) and Eddington ratios ($\lambda_{\rm Edd}$) of six confirmed CL-AGNs (Table 2) as well as those of four CL-AGNs reported in Zhu et al. (2025), are shown in Fig. 5. For comparison, the values of the CL-AGN sample reported by Guo et al. (2025) are also plotted in the figure. This currently largest CL-AGN sample was built by comparing spectrum data from SDSS and DESI. The ten CL-AGNs identified from the CM variability pattern method are in ranges of $\log(M_{\rm BH}/M_\odot) \sim 6.9$ to 9.0 and $\log \lambda_{\rm Edd} \sim -2.4$ to -1.4. Thus, these ten AGNs generally have $\lambda_{\rm Edd}$ values at the low end. This feature of low $\lambda_{\rm Edd}$ values has also been noted, for example, in extreme variability quasars ((Rumbaugh et al. 2018)) and in CL quasars (MacLeod et al. 2019).

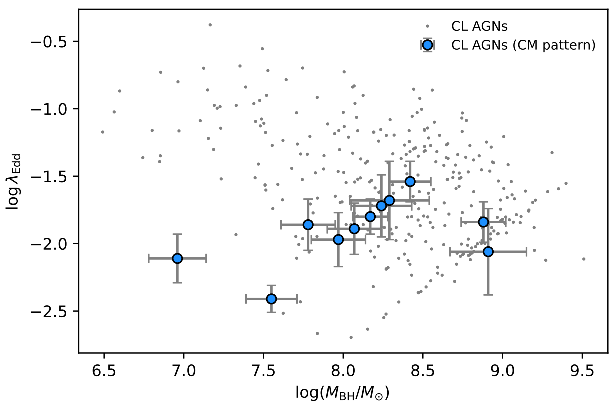

Fig. 5: Distribution of black hole masses ($M_{\rm BH}$) versus Eddington ratios ($\lambda_{\rm Edd}$) for the CL-AGNs identified via the CM variability method. The data points comprise six confirmed sources from this work and the four sources previously reported in Zhu et al. (2025). The background data points are the CL-AGNs reported by Guo et al. (2025).

4. Discussion

Following our CM variability method established in Zhu et al. (2025), we carried out further studies and observed another 12 sources in 2024–2025. Seven of them were confirmed as CL-AGNs (though two of them have already been reported in Guo et al. 2025). A detailed examination of the unconfirmed candidates has revealed that several factors may hinder the successful identification of a CL transition. First, most of the candidates were selected because they recently exhibited variations of a flare-like event (e.g., Fig. 1 and B.5) and the BWB pattern was dominantly established by this event (Fig. D.1), and thus the time lag between the photometric flare and the spectroscopic follow-up could be critical. For instance, J111614+061736 (Fig. C.4) was observed ~4 years after its light curve peak, potentially causing the broad-line emergence window to be missed. This might have also occurred in the unconfirmed cases of J1246−0156, J1252+0717, and J1423+2454 reported in Zhu et al. (2025). Second, data quality can affect the results. The DOT spectra suffer from large uncertainties in the blue part, which is particularly severe for the identification of broad lines in J105344+492955 (Fig. C.2). Similarly, the DOT spectrum of J111137+140118 (Fig. C.3) exhibited a significant strengthening of broad Hα, yet it lacked the unambiguous emergence of broad Hβ; thus, we conservatively excluded it from our turn-on sample. Third, careful examination of J132558+411500's light curves and spectra (Fig. C.5) made us realize that it is likely a blazar, as it exhibited large daily optical variations (over 1 mag), nearly simultaneous fast flux variations in MIR bands, and flat continuum plus weak lines. Indeed, it is identified as a blazar of the BL Lacertae type (4FGL J1326.2+4115 or IVS B1323+415) in the Fermi Large Area Telescope (LAT) catalog (Ballet et al. 2023). A lesson we learned is that our selection of candidates requires further checking of multiband information in order to exclude such sources as this blazar.

While this work proves again that the CM variability pattern method can effectively find turn-on CL-AGNs, the candidates we selected approximately belong to the extreme variability quasar type, i.e., AGNs showing $\geq$ 1 mag changes (Rumbaugh et al. 2018; Ren et al. 2022). In the selection of this work, we also considered the MIR variations ($\Delta W2 > 0.4$) and the clear BWB pattern ($k \geq 0.1$). Among the 12923 SDSS Type-2 AGNs, there were 42 satisfying these requirements. Because we have access to 2- and 3-meter telescopes for spectroscopic observations, the targets selected were relatively bright, with averaged zg magnitudes smaller than 19.5. This brightness requirement excludes seven faint sources. Among the remaining 35 Type-2 AGNs, we observed 17, of which 12 were identified as CL-AGNs (including five from Zhu et al. 2025). Therefore, when a previously identified Type-2 AGN shows large BWB flux variations, it is highly likely that it would have undergone a CL transition. The cause of the large variations in several of our cases was several-years-long flare-like events, which may provide a clue to understanding the CL process. One possible scenario is that if there is a denser part of the inflow reaching the inner disk, the accretion rate rises in a short time, producing a brighter optical/UV continuum and more ionizing photons (Dexter & Agol 2011; Dexter & Begelman 2019; Sniegowska et al. 2020). The stronger ionizing continuum illuminates more BLR gas, so the effective BLR size increases, as expected from the BLR radius–luminosity relation and BLR breathing behavior (Bentz et al. 2013; Goad & Korista 2014). Since broad Hα is usually stronger and may arise from a slightly larger lower-ionization region than broad Hβ, an early or weak turn-on phase may show broad Hα, while broad Hβ is still weak or absent (similar to Seyfert Type 1.8/1.9; Osterbrock 1981; Winkler 1992). This early turn-on of broad Hα was possibly seen in J131101+000310 (Fig. B.3) and J134330+510204 (Fig. B.4). In this sense, the method we used would preferentially select high-variability recent turn-on CL events, in which the flare-like events serve as an observational sign for the accretion enhancement in the central engine.

The relatively low Eddington ratios of these CL-AGNs (Fig. 5) may suggest that their previous Type 2 classification was intrinsic, consistent with the concept of "naked" Type-2 AGNs (Yang et al. 2023). In such AGNs, BELs are absent, yet no obscuration is detected in X-ray observations (LaMassa et al. 2014; Jana et al. 2025). These CL-AGNs showed MIR variabilities that closely follow the optical variations, indicating the absence of obscuration along the line of sight. The absence of BELs in them was thus likely due to a low accretion rate that is insufficient to sustain a visible BLR. In comparison to the larger sample from Chen et al. (2025), whose $\log \lambda_{\rm Edd}$ span from ~ -3.2 to -0.8 (see also Panda & Śniegowska 2024; Zeltyn et al. 2024; Yang et al. 2025 for similarly broad distributions), these CL-AGNs show a narrow distribution clustered around the critical value of $\log \lambda_{\rm Edd} \approx -2$, which may imply that they represent a transitional group between the low-accretion Type-2 phase and the high-accretion Type-1 phase. Since $\log \lambda_{\rm Edd} \sim -2$ is generally considered to represent the theoretical boundary between the advection-dominated accretion flow (ADAF) and the standard Shakura-Sunyaev disk (SSD; Noda & Done 2018), this clustering suggests that these sources were likely not in a stable accretion mode but rather in a pivotal state between the ADAF and SSD modes.

As the CL-AGN population continues to expand, a variety of mechanisms have been proposed. For example, there are scenarios of varying obscuration caused by disk winds or outflows (e.g., Elitzur 2012; Gaskell & Harrington 2018), the presence of SMBH binaries that perturb the accretion flow (Wang & Bon 2020), the propagation of cooling fronts within the accretion disk (Ross et al. 2018), the inefficient cooling of hot outflows from ADAFs preventing BLR formation (Cao 2010), and magnetic or radiation pressure instabilities triggering rapid luminosity changes (e.g., Dexter & Begelman 2019; Sniegowska et al. 2020). It is likely because of the finding method we used that the CL-AGNs in our sample appear to fit in the accretion-mode transition scenario. However, even within this framework, different triggers may be at play. For instance, tidal disruption events in AGNs can fuel a sudden, dramatic brightening (e.g., Trakhtenbrot et al. 2019; Blanchard et al. 2017). Alternatively, Kaaz et al. (2025) proposed that lense-thirring precession in a misaligned accretion disk can lead to "disk tearing," causing rapid infall of material and triggering a CL transition. Crucially, this mechanism is sensitive to the accretion rate. At the critical rate of $\lambda_{\rm Edd} \sim 0.01$, the disk is susceptible to tearing, potentially turning the BLR on or off completely. Finally, drawing an analogy to stellar-mass BH systems offers a unifying perspective. Such studies (e.g., Ruan et al. 2019; liu et al. 2019; Ai et al. 2020; Gilbert et al. 2025) have linked the CL-AGN phenomenon to the high-soft–low-hard state transitions observed in X-ray binaries. This scale-invariant view suggests that the physics of accretion flow changes—driven by the interplay among the components, disk, corona, and jet—may be fundamental across all mass scales, providing a robust framework for understanding the extreme-variability–related CL transitions.

Data availability

The reduced spectra obtained in this work are available in electronic form at the CDS via anonymous ftp to cdsarc.u-strasbg.fr (130.79.128.5) or via http://cdsweb.u-strasbg.fr/cgi-bin/qcat?J/A+A/.

Acknowledgements. This work was based on observations obtained with the Samuel Oschin Telescope 48-inch and the 60-inch Telescope at the Palomar Observatory as part of the Zwicky Transient Facility project. ZTF is supported by the National Science Foundation under Grant No. AST-2034437 and a collaboration including Caltech, IPAC, the Weizmann Institute for Science, the Oskar Klein Center at Stockholm University, the University of Maryland, Deutsches Elektronen-Synchrotron and Humboldt University, the TANGO Consortium of Taiwan, the University of Wisconsin at Milwaukee, Trinity College Dublin, Lawrence Livermore National Laboratories, and IN2P3, France. Operations are conducted by COO, IPAC, and UW.
This study makes use of data obtained from the 2-m Himalayan Chandra Telescope (HCT). We thank the staff at IAO, Hanle, and CREST, Hosakote, operated by the Indian Institute of Astrophysics, Bengaluru (India), for their support in facilitating these observations.
This work is based on observations obtained at the 3.6m Devasthal Optical Telescope (DOT), which is a National Facility run and managed by Aryabhatta Research Institute of Observational Sciences (ARIES), an autonomous Institute under the Department of Science and Technology, Government of India.
Funding for the Sloan Digital Sky Survey V has been provided by the Alfred P. Sloan Foundation, the Heising-Simons Foundation, the National Science Foundation, and the Participating Institutions. SDSS acknowledges support and resources from the Center for High-Performance Computing at the University of Utah. SDSS telescopes are located at Apache Point Observatory, funded by the Astrophysical Research Consortium and operated by New Mexico State University, and at Las Campanas Observatory, operated by the Carnegie Institution for Science. The SDSS web site is www.sdss.org.
SDSS is managed by the Astrophysical Research Consortium for the Participating Institutions of the SDSS Collaboration, including the Carnegie Institution for Science, Chilean National Time Allocation Committee (CNTAC) ratified researchers, Caltech, the Gotham Participation Group, Harvard University, Heidelberg University, The Flatiron Institute, The Johns Hopkins University, L'Ecole polytechnique fédérale de Lausanne (EPFL), Leibniz-Institut für Astrophysik Potsdam (AIP), Max-Planck-Institut für Astronomie (MPIA Heidelberg), Max-Planck-Institut für Extraterrestrische Physik (MPE), Nanjing University, National Astronomical Observatories of China (NAOC), New Mexico State University, The Ohio State University, Pennsylvania State University, Smithsonian Astrophysical Observatory, Space Telescope Science Institute (STScI), the Stellar Astrophysics Participation Group, Universidad Nacional Autónoma de México, University of Arizona, University of Colorado Boulder, University of Illinois at Urbana-Champaign, University of Toronto, University of Utah, University of Virginia, Yale University, and Yunnan University.
This publication makes use of data products from the Wide-field Infrared Survey Explorer, which is a joint project of the University of California, Los Angeles, and the Jet Propulsion Laboratory/California Institute of Technology, funded by the National Aeronautics and Space Administration. This publication also makes use of data products from NEOWISE, which is a project of the Jet Propulsion Laboratory/California Institute of Technology, funded by the Planetary Science Division of the National Aeronautics and Space Administration.
This work has made use of data from the Asteroid Terrestrial-impact Last Alert System (ATLAS) project. The Asteroid Terrestrial-impact Last Alert System (ATLAS) project is primarily funded to search for near earth asteroids through NASA grants NN12AR55G, 80NSSC18K0284, and 80NSSC18K1575; byproducts of the NEO search include images and catalogs from the survey area. This work was partially funded by Kepler/K2 grant J1944/80NSSC19K0112 and HST GO-15889, and STFC grants ST/T000198/1 and ST/S006109/1. The ATLAS science products have been made possible through the contributions of the University of Hawaii Institute for Astronomy, the Queen's University Belfast, the Space Telescope Science Institute, the South African Astronomical Observatory, and The Millennium Institute of Astrophysics (MAS), Chile.
This work made use of the data from LAMOST (Large Sky Area Multi-Object Fiber Spectroscopic Telescope, also known as the Guoshoujing Telescope) (https://cstr.cn/31118.02.LAMOST). LAMOST is a Chinese national mega-science facility, operated by National Astronomical Observatories, Chinese Academy of Sciences.
This work made use of data from the Catalina Real-time Transient Survey, which is based on data obtained by the Catalina Sky Survey. The Catalina Sky Survey is funded by NASA under the Near Earth Object Observations Program.
This research is supported by the National Natural Science Foundation of China (12273033) and the Xingdian Talent Support Project of the Yunnan Province (XDYC-YLXZ-2023-0016)

References

Abazajian, K. N., Adelman-McCarthy, J. K., Agüeros, M. A., et al. 2009, ApJS, 182, 543
Ahumada, R., Prieto, C. A., Almeida, A., et al. 2020, The Astrophysical Journal Supplement Series, 249, 3
Ai, Y., Dou, L., Yang, C., et al. 2020, ApJ, 890, L29
Antonucci, R. 1993, ARA&A, 31, 473
Aretxaga, I., Joguet, B., Kunth, D., Melnick, J., & Terlevich, R. J. 1999, ApJ, 519, L123
Ballet, J., Bruel, P., Burnett, T. H., Lott, B., & The Fermi-LAT collaboration. 2023, arXiv e-prints, arXiv:2307.12546
Bellm, E. C., Kulkarni, S. R., Graham, M. J., et al. 2019, PASP, 131, 018002
Bentz, M. C., Denney, K. D., Grier, C. J., et al. 2013, ApJ, 767, 149
Blanchard, P. K., Nicholl, M., Berger, E., et al. 2017, ApJ, 843, 106
Cao, X. 2010, ApJ, 724, 855
Chen, Z.-Q., Jin, J.-J., Guo, W.-J., et al. 2025, arXiv e-prints, arXiv:2511.15359
Cohen, R. D., Rudy, R. J., Puetter, R. C., Ake, T. B., & Foltz, C. B. 1986, ApJ, 311, 135
Cowsik, R., Srinivasan, R., & Prabhu, T. P. 2002, Bulletin of the Astronomical Society of India, 30, 105
Cui, X.-Q., Zhao, Y.-H., Chu, Y.-Q., et al. 2012, Research in Astronomy and Astrophysics, 12, 1197
Denney, K. D., De Rosa, G., Croxall, K., et al. 2014, ApJ, 796, 134
DESI Collaboration, Aghamousa, A., Aguilar, J., et al. 2016, arXiv e-prints, arXiv:1611.00036
Dexter, J. & Agol, E. 2011, ApJ, 727, L24
Dexter, J. & Begelman, M. C. 2019, MNRAS, 483, L17
Dong, Q., Zhang, Z.-X., Gu, W.-M., Sun, M., & Zheng, Y.-G. 2025, ApJ, 986, 160
Drake, A. J., Djorgovski, S. G., Mahabal, A., et al. 2009, ApJ, 696, 870
Elitzur, M. 2012, ApJ, 747, L33
Eracleous, M. & Halpern, J. P. 2001, ApJ, 554, 240
Frederick, S., Gezari, S., Graham, M. J., et al. 2019, ApJ, 883, 31
Fu, Y. 2021, QSOFITMORE: a python package for fitting UV-optical spectra of quasars
Gaskell, C. M. & Harrington, P. Z. 2018, MNRAS, 478, 1660
Gezari, S., Hung, T., Cenko, S. B., et al. 2017, ApJ, 835, 144
Gilbert, O., Ruan, J. J., Duffy, L., et al. 2025, arXiv e-prints, arXiv:2508.01933
Goad, M. R. & Korista, K. T. 2014, MNRAS, 444, 43
Graham, M. J., Ross, N. P., Stern, D., et al. 2020, MNRAS, 491, 4925
Green, P. J., Pulgarin-Duque, L., Anderson, S. F., et al. 2022, ApJ, 933, 180
Guo, H., Shen, Y., & Wang, S. 2018, PyQSOFit: Python code to fit the spectrum of quasars, Astrophysics Source Code Library, record ascl:1809.008
Guo, W.-J., Zou, H., Fawcett, V. A., et al. 2024, ApJS, 270, 26
Guo, W.-J., Zou, H., Greenwell, C. L., et al. 2025, ApJS, 278, 28
Jana, A., Ricci, C., Temple, M. J., et al. 2025, A&A, 693, A35
Kaaz, N., Liska, M., Ward, C., & Davelaar, J. 2025, arXiv e-prints, arXiv:2511.09626
LaMassa, S. M., Cales, S., Moran, E. C., et al. 2015, ApJ, 800, 144
LaMassa, S. M., Yaqoob, T., Ptak, A. F., et al. 2014, ApJ, 787, 61
Lawrence, A. 1987, PASP, 99, 309
Lawrence, A. 2018, Nature Astronomy, 2, 102
Liu, C., Kong, F., Cooper, E. M., et al. 2026, ApJS, 284, 12
liu, H., Wu, Q., Lyu, B., & Yan, Z. 2019, arXiv e-prints, arXiv:1912.03972
López-Navas, E., Martínez-Aldama, M. L., Bernal, S., et al. 2022, MNRAS, 513, L57
López-Navas, E., Sánchez-Sáez, P., Arévalo, P., et al. 2023, MNRAS, 524, 188
MacLeod, C. L., Green, P. J., Anderson, S. F., et al. 2019, ApJ, 874, 8
MacLeod, C. L., Ross, N. P., Lawrence, A., et al. 2016, MNRAS, 457, 389
Mainzer, A., Bauer, J., Grav, T., et al. 2011, ApJ, 731, 53
Noda, H. & Done, C. 2018, MNRAS, 480, 3898
Omar, A., Kumar, T. S., Krishna Reddy, B., Pant, J., & Mahto, M. 2019, arXiv e-prints, arXiv:1902.05857
Osterbrock, D. E. 1981, ApJ, 249, 462
Panda, S. & Śniegowska, M. 2024, ApJS, 272, 13
Planck Collaboration, Aghanim, N., Akrami, Y., et al. 2020, A&A, 641, A6
Ren, W., Wang, J., Cai, Z., & Guo, H. 2022, ApJ, 925, 50
Richards, G. T., Lacy, M., Storrie-Lombardi, L. J., et al. 2006, ApJS, 166, 470
Ross, N. P., Ford, K. E. S., Graham, M., et al. 2018, MNRAS, 480, 4468
Ross, N. P., Graham, M. J., Calderone, G., et al. 2020, MNRAS, 498, 2339
Ruan, J. J., Anderson, S. F., Cales, S. L., et al. 2016, ApJ, 826, 188
Ruan, J. J., Anderson, S. F., Eracleous, M., et al. 2019, ApJ, 883, 76
Rumbaugh, N., Shen, Y., Morganson, E., et al. 2018, ApJ, 854, 160
Runnoe, J. C., Cales, S., Ruan, J. J., et al. 2016, MNRAS, 455, 1691
Scargle, J. D., Norris, J. P., Jackson, B., & Chiang, J. 2013, ApJ, 764, 167
Shappee, B. J., Prieto, J. L., Grupe, D., et al. 2014, ApJ, 788, 48
Sheng, Z., Wang, T., Jiang, N., et al. 2020, ApJ, 889, 46
Sniegowska, M., Czerny, B., Bon, E., & Bon, N. 2020, A&A, 641, A167
Storchi-Bergmann, T., Baldwin, J. A., & Wilson, A. S. 1993, ApJ, 410, L11
Tadhunter, C. 2008, New A Rev., 52, 227
Tohline, J. E. & Osterbrock, D. E. 1976, ApJ, 210, L117
Tonry, J. L., Denneau, L., Heinze, A. N., et al. 2018, PASP, 130, 064505
Trakhtenbrot, B., Arcavi, I., MacLeod, C. L., et al. 2019, ApJ, 883, 94
Urry, C. M. & Padovani, P. 1995, PASP, 107, 803
Verrico, M. E., French, K. D., Baldassare, V. F., et al. 2026, ApJ, 1004, 121
Vestergaard, M. & Peterson, B. M. 2006, ApJ, 641, 689
Wang, J., Zheng, W. K., Brink, T. G., et al. 2023, ApJ, 956, 137
Wang, J.-M. & Bon, E. 2020, A&A, 643, L9
Wang, S., Woo, J.-H., Gallo, E., et al. 2024, ApJ, 966, 128
Winkler, H. 1992, MNRAS, 257, 677
WISE Team. 2020, NEOWISE 2-Band Post-Cryo Single Exposure (L1b) Source Table
Wright, E. L., Eisenhardt, P. R. M., Mainzer, A. K., et al. 2010, AJ, 140, 1868
Yang, Q., Green, P., Wu, X.-B., et al. 2025, in American Astronomical Society Meeting Abstracts, Vol. 245, American Astronomical Society Meeting Abstracts #245, 221.06
Yang, Q., Green, P. J., MacLeod, C. L., et al. 2023, ApJ, 953, 61
Yang, Q., Wu, X.-B., Fan, X., et al. 2018, ApJ, 862, 109
Zeltyn, G., Trakhtenbrot, B., Eracleous, M., et al. 2024, ApJ, 966, 85
Zhu, L.-T., Li, J., Wang, Z., & Zhang, J.-J. 2024, MNRAS, 530, 3538
Zhu, L.-T., Wang, Z., Devanand, P. U., et al. 2025, MNRAS, 536, 2715

Appendix A: Information for the DOT and HCT spectroscopic observations of the 12 candidates

Table A.1: Information for the DOT and HCT observations.

Name	R.A.	Dec.	Standard	Observation
Confirmed CL AGN				
J014638+131109	26.6620	13.1859	G19B2B	2024-12-23/HCT
J115953+051330	179.9725	5.2250	Feige34	2025-01-25/DOT
J121228+501412	183.1187	50.2367	Feige66	2025-03-24/HCT
J131101+000310	197.7551	0.0530	Feige34	2025-01-24/DOT
J134330+510204	205.8751	51.0345	Feige34	2025-01-23/DOT
J152502+110744	231.2622	11.1289	HZ44	2025-05-28/HCT
J160626+044802	241.6099	4.8006	Feige66	2025-03-24/HCT
Other candidate				
J075846+270515	119.6958	27.0877	G19B2B	2024-12-23/HCT
J111614+061736	169.0611	6.29335	Feige66	2025-03-24/HCT
J105344+492955	163.4339	49.4989	Feige34	2025-01-21/DOT
J111137+140118	167.9066	14.0217	Feige34	2025-01-23/DOT
J132558+411500	201.4956	41.2501	HZ44	2025-05-28/HCT

Appendix B: Light curves and spectra of seven CL AGNs

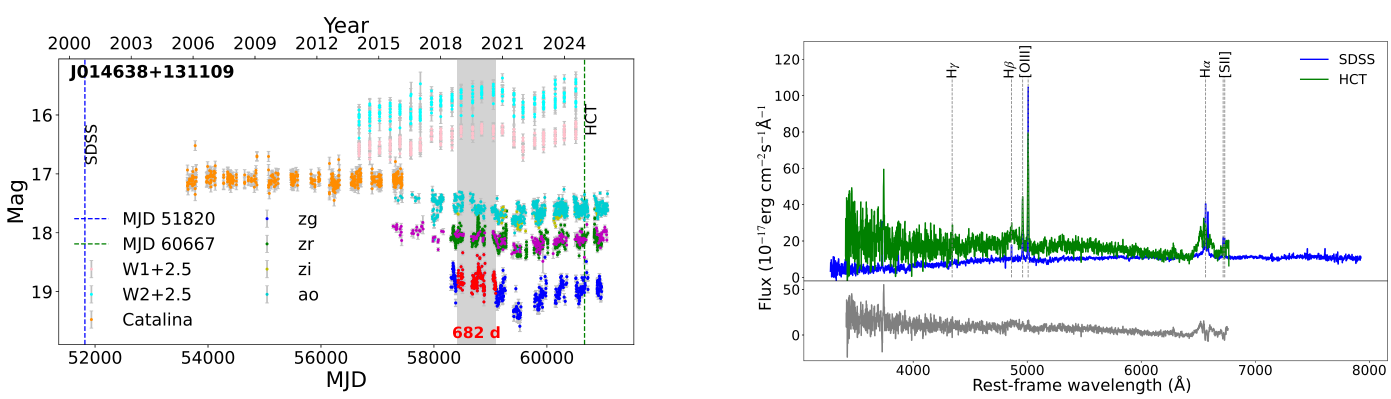

Fig. B.1: Same as Fig. 1 but for J014638+131109.

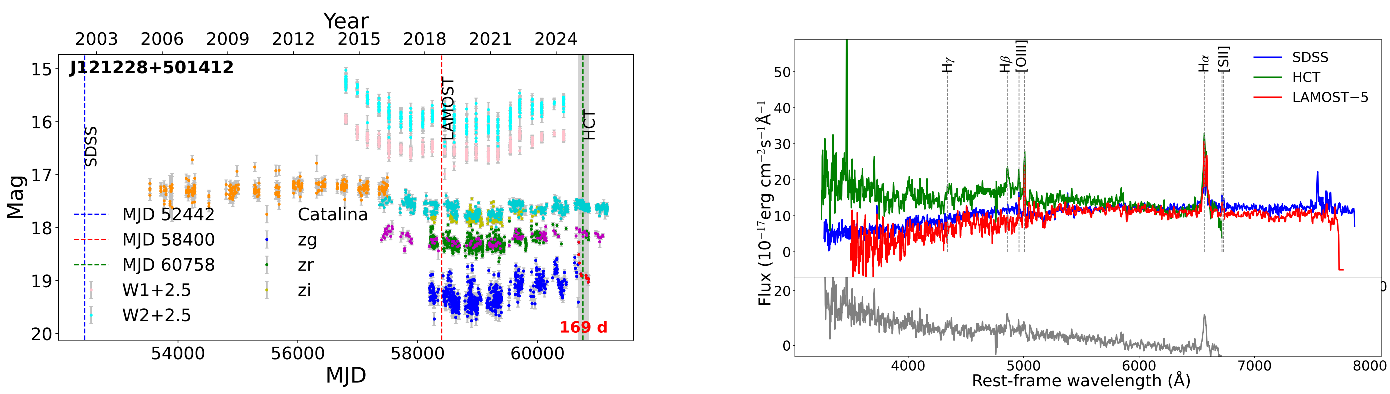

Fig. B.2: Same as Fig. 1 but for J121228+501412.

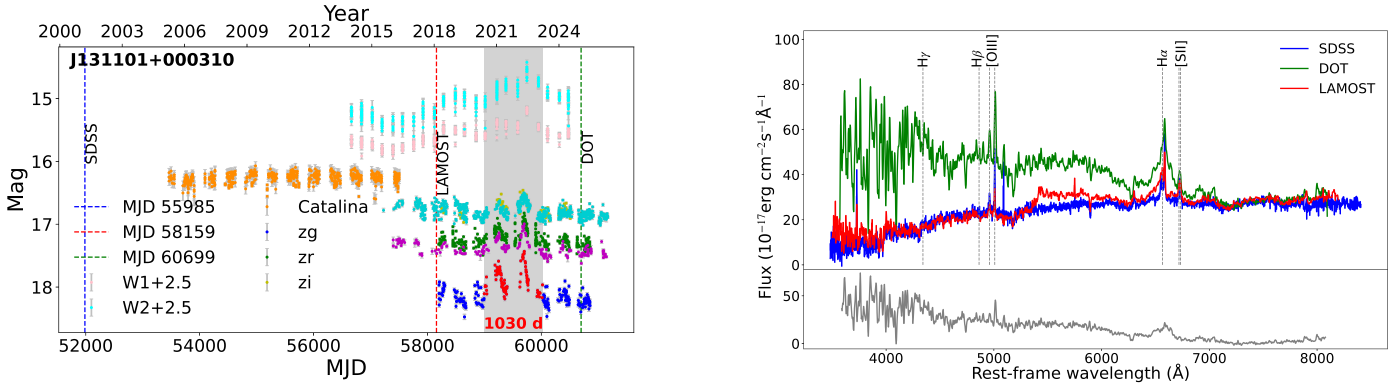

Fig. B.3: Same as Fig. 2 but for J131101+000310.

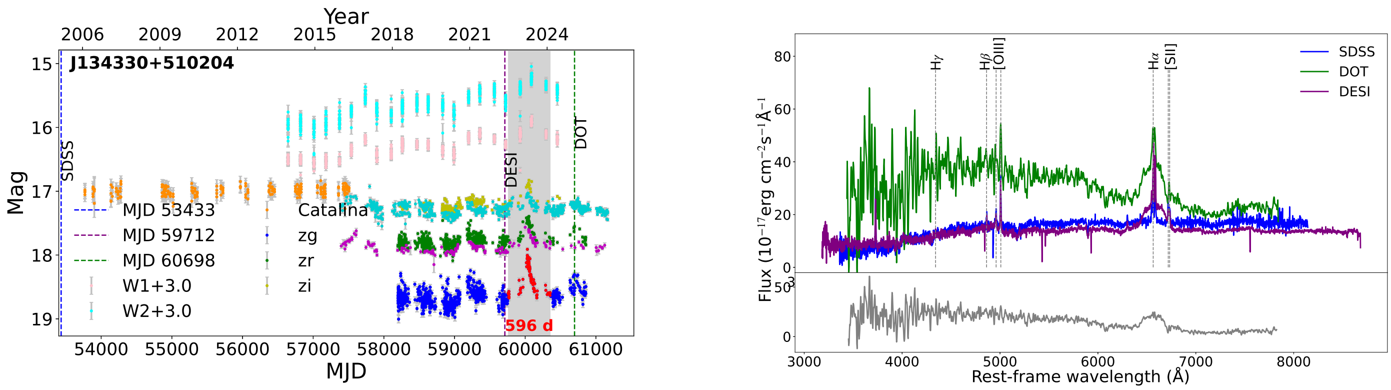

Fig. B.4: Same as Fig. 2 but for J134330+510204.

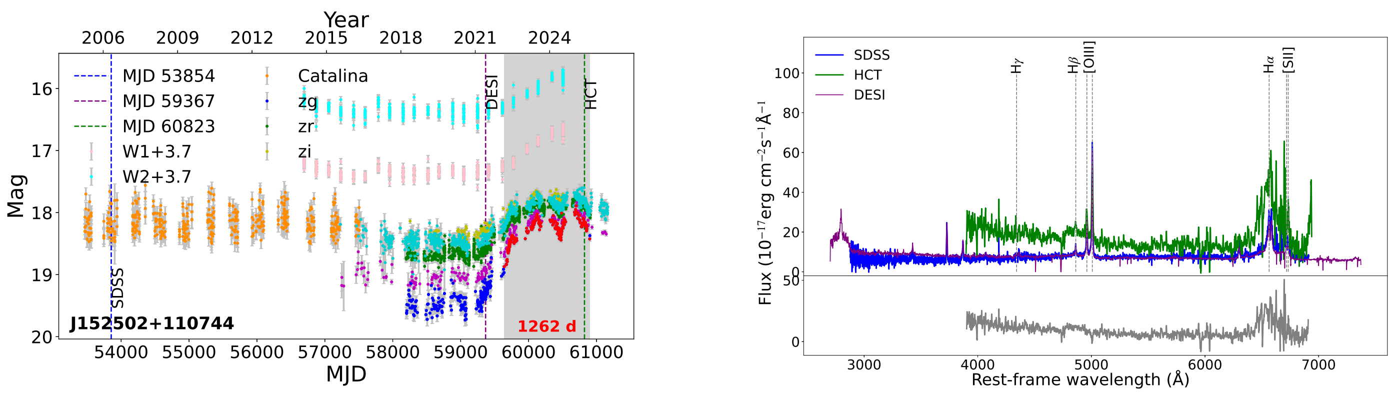

Fig. B.5: Same as Fig. 1 but for J152502+110744.

Appendix C: Light curves and spectra of five other candidates

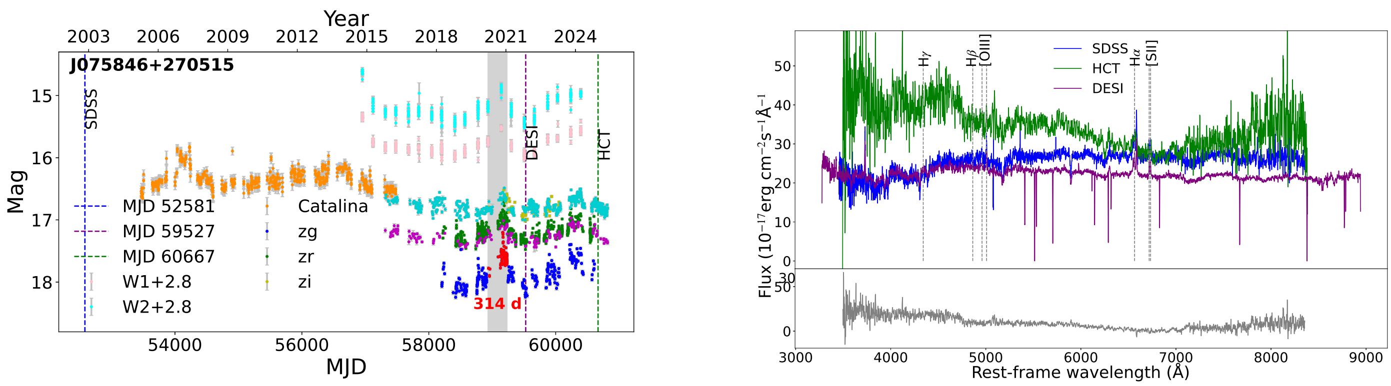

Fig. C.1: Same as Fig. 1 but for the non-confirmed CL candidate J075846+270515.

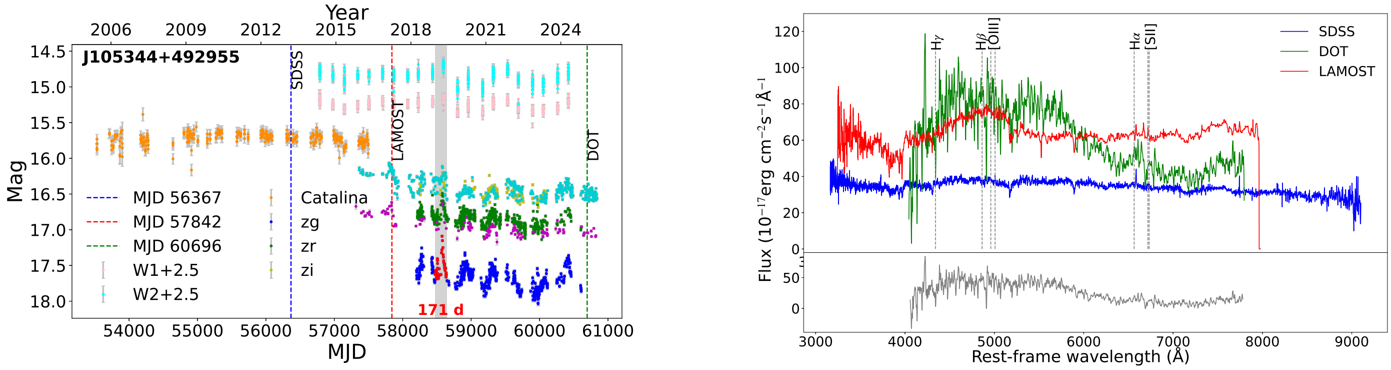

Fig. C.2: Same as Fig. 2 but for the non-confirmed CL candidate J105344+492955.

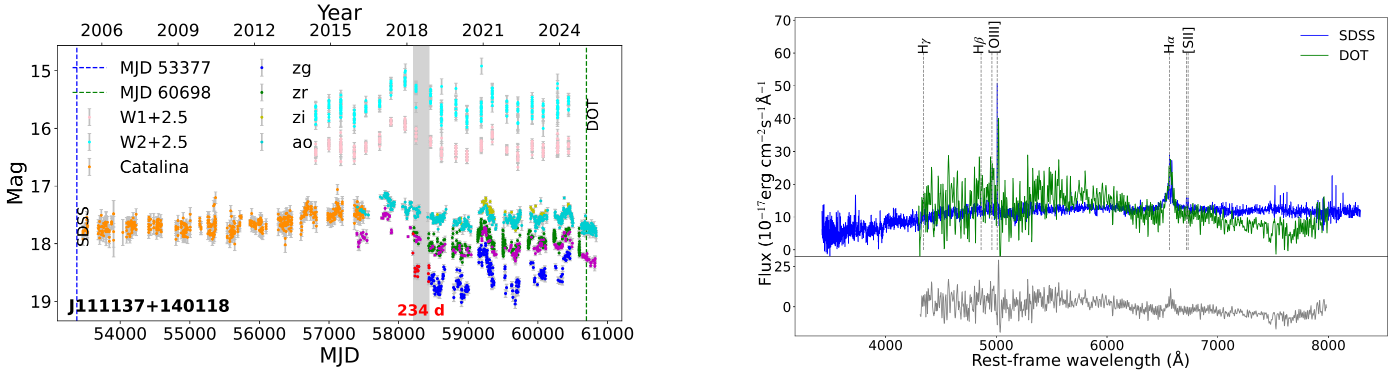

Fig. C.3: Same as Fig. 2 but for the non-confirmed CL candidate J111137+140118.

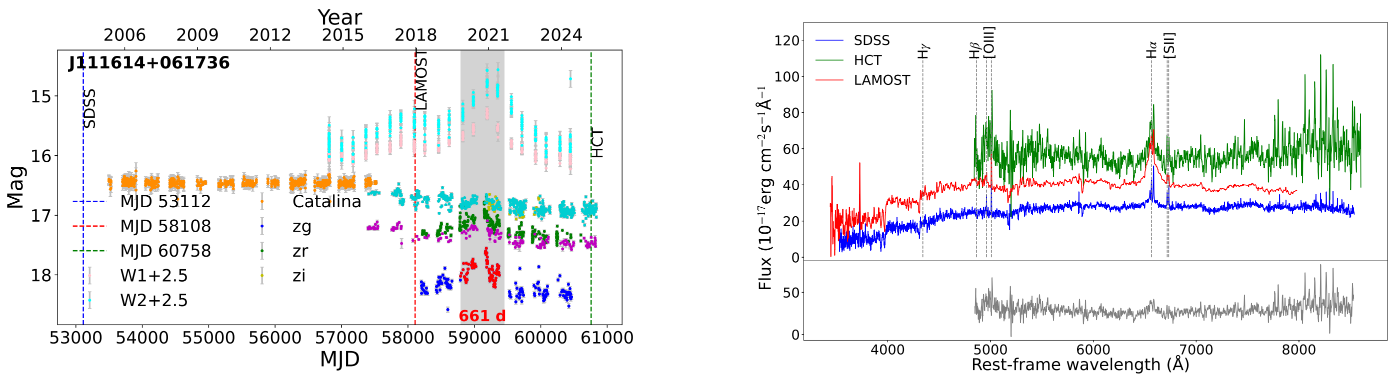

Fig. C.4: Same as Fig. 1 but for the non-confirmed CL candidate J111614+061736.

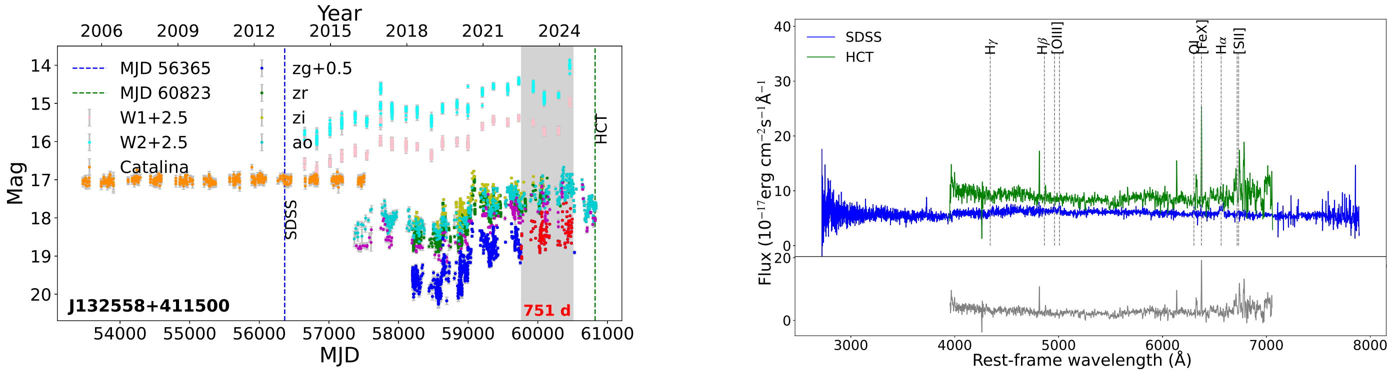

Fig. C.5: Same as Fig. 1 but for the non-confirmed CL candidate J132558+411500.

Appendix D: CM diagrams of 12 AGN targets

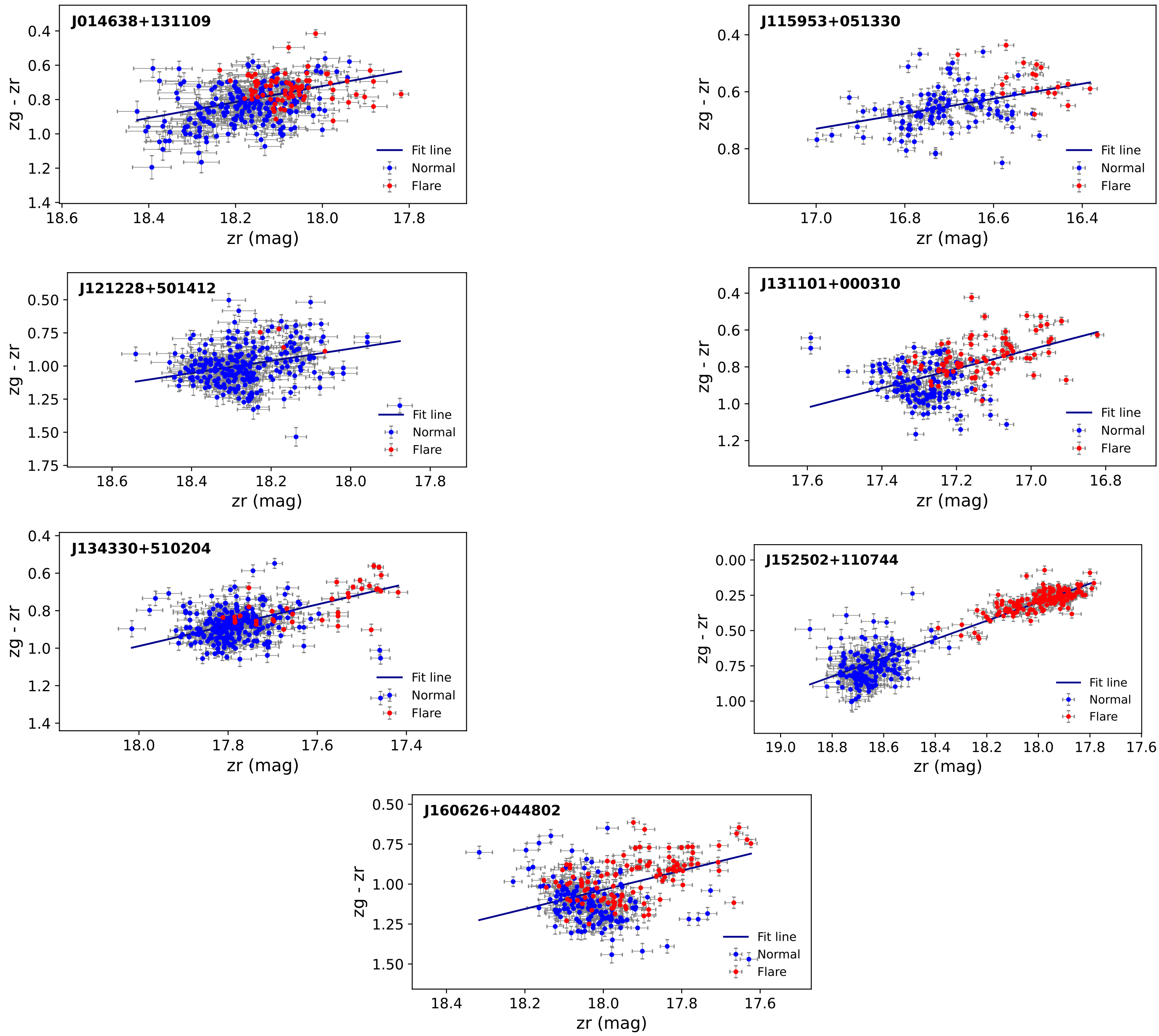

Fig. D.1: Color–magnitude diagrams of seven CL-AGNs: J014638+131109, J115953+051330, J121228+501412, J131101+000310, J134330+510204, J152502+110744, and J160626+044802.

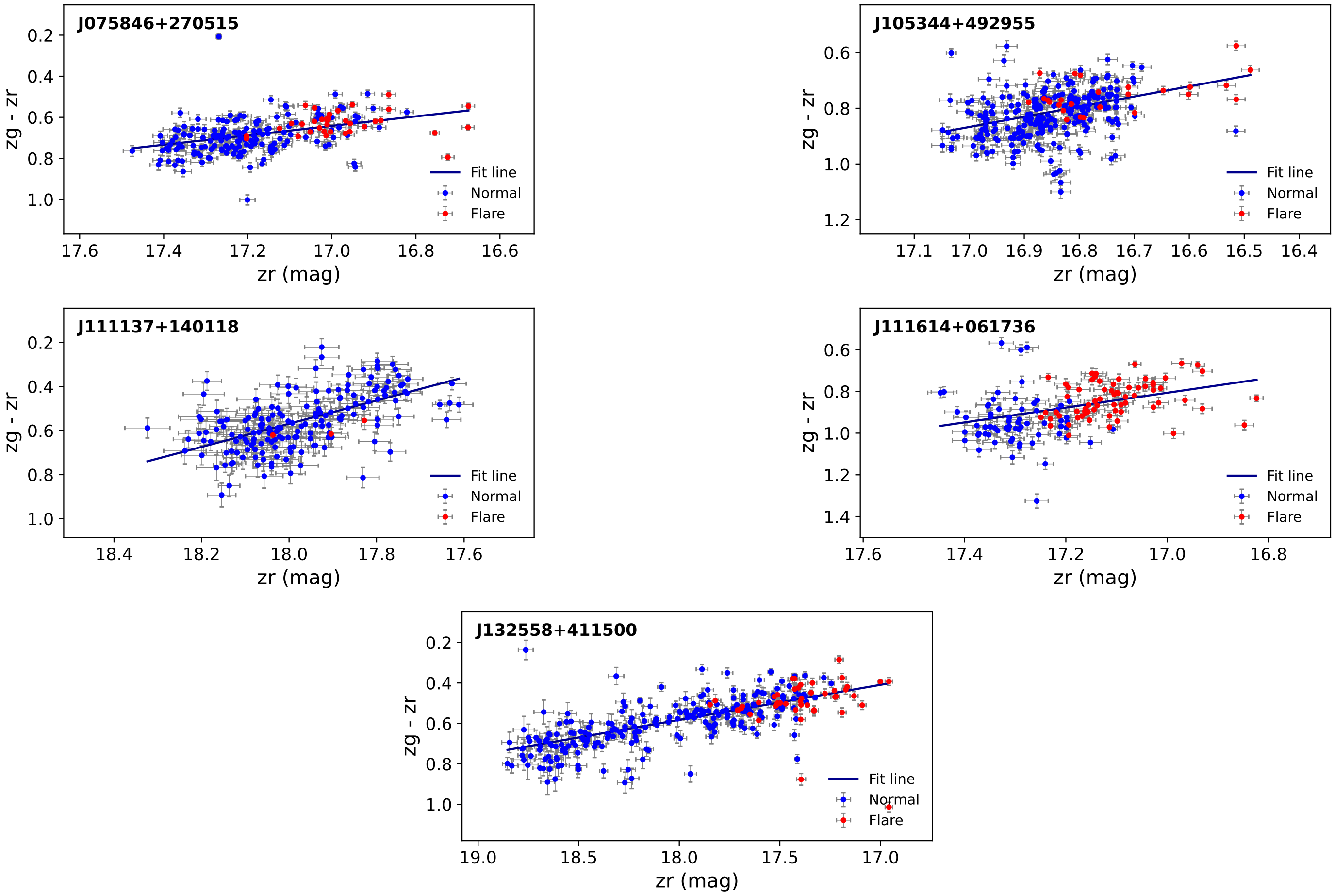

Fig. D.2: Color–magnitude diagrams of five not confirmed CL-AGN candidates: J075846+270515, J105344+492955, J111137+140118, J111614+061736, and J132558+411500.